Mechatronics of Electrostatic Microactuators for Computer Disk Drive Dual-Stage Servo Systems

Yunfeng Li, *Student Member, IEEE,* and Roberto Horowitz, *Member, IEEE*

Abstract—A decoupled control design structure and discrete time pole placement design method are proposed for MEMS-based dual-stage servo control design in magnetic disk drives. Dual-stage track following controllers are designed using a decoupled three-step design process: the voice coil motor (VCM) loop design, the microactuator (MA) inner loop design, and the MA outer loop design. Both MIMO (when the MA relative position sensing is available) and SIMO (when the MA relative position sensing is not available) designs are considered. The effect of MA resonance mode variations on the stability and performance of the controllers are analyzed. Self-tuning control and online identification of the MA model are developed to compensate for the variations in the MA's resonance mode.

Index Terms—Dual stage, hard disk drive, servo control.

I. INTRODUCTION

I T IS predicted that future areal storage density increases in magnetic disk drive will be achieved mainly through an increase in track density. For a predicted bit aspect ratio of 4:1, an areal density of 100 Gb/in^2 translates to a linear bit density of 672k bits per inch (BPI), and a radial track density of 168k tracks per inch (TPI), which in turn implies a track pitch of 150 nm. In order to achieve an ultimate tenfold increase in TPI, it will be necessary to develop high-bandwidth, robust track-following servo systems. Dual-stage actuation has been proposed as a means of attaining the necessary servo bandwidth to achieve the required runout and disturbances rejections.

Two dual-stage actuation approaches for magnetic disk drives are currently being considered by the magnetic recording industry. In the first approach, which is generally referred to as the actuated suspension, mini-actuators (usually made of piezoelectric materials such as PZT) are used to flex the suspension around a pivot, producing relative motion of the read/write head along the radial direction. However, most actuated suspensions have multiple structural resonance modes in the 4–12-kHz frequency range, which may limit the bandwidth of the servo system. The second approach to dual-stage actuation utilizes micro-electromechanical systems (MEMS) and is generally referred to as the actuated slider approach [1], [2]. In this approach, an electrostatic or electromagnetic MEMS fabricated microactuator (MA) is sandwiched between the gimbal and the

slider, and it either rotates or translates the slider relative to the suspension. The actuated slider approach achieves a truly collocated second stage actuation of the read/write head, by-passing nonlinear friction, bias forces, and all E-block, suspension, and gimbal structural resonance modes. Usually, a MEMS MA has a single flexure resonance mode in the 1–2-kHz frequency range and has no other appreciable structural resonance modes up the 40-kHz frequency range [1], [3]. Thus, the MEMS MA actuated slider dual-stage approach may provide a potential high-performance and low-cost solution to achieving extremely high track density, since the MEMS MA can be batch-fabricated and micro-assembled with the head and the gimbal of suspension.

The resonance frequency of the MEMS MA's lightly damped flexure resonance mode is relatively low and close to the open loop gain crossover frequency of the servo system. Furthermore, due to lithographic misalignment and variations present in the etching processes, the actual resonance frequency of the MA can vary by as much as $\pm 15\%$ from its designed nominal value. Thus, the controller robustness to the uncertainty in the MA's resonance frequency must be considered for MEMS-based dual-stage servo control design. Another difference between PZT actuated suspension and the MEMS-based dual-stage system is the availability of the sensor that can measure the displacement of the read/write head, relative to the suspension. In most PZT actuated suspensions, relative position sensing is generally not available and the dual-stage controller must be single-input–multi-output (SIMO), while, for most MEMS MAs, capacitive or piezoresistive sensing can be used to measure the MA's relative position [2], and the dual-stage controller can potentially be multi-input–multi-output (MIMO).

Several controller design methods have been proposed for PZT actuated suspension dual-stage systems [4]–[7]. Controller designs for MEMS-based dual-stage servo systems have been reported in [8] and [9]. In [8], a SIMO controller was designed using a parallel design technique. However, the robustness of the servo system to variations in the microactuator resonance mode was not addressed. In [9], robust SIMO and MIMO H_∞ optimal controllers were designed using μ-synthesis. In this paper, we present a decoupled discrete time pole placement design method which can be used for both SIMO and MIMO controller designs. The decoupling design approach utilized in this paper was originally introduced in [10], for use in a PZT actuated suspension. Compared with the μ-synthesis design in [9], the implementation of the controller designed using this method requires significantly less computations. Moreover, decoupled pole placement design can be combined with a self-tuning or an online

Fig. 1. IBM's electrostatic MA mounted on an integrated lead suspension (Courtesy of L.-S. Fan.).

identification scheme for compensating variations in the MA's resonance frequency.

The paper is organized as follows. A MEMS-based dual-stage actuator model is briefly introduced in Section II. In Section III, the decoupled controller design structure and discrete time sensitivity transfer function design process are presented. The robustness of the designs is analyzed in Section IV using μ-analysis. In Section V, MA inner-loop self-tuning control and online identification of the MA model parameters for compensating the MA's resonance mode variations are discussed. Conclusions are provided in Section VI.

II. DUAL-STAGE MODEL WITH A MEMS MA

Fan and co-workers at the IBM Almaden Research Center (ARC) have developed an innovative etching and electroplating multilayer technology for fabricating high-aspect-ratio MEMS devices [1]. This fabrication process can be implemented at IBM's existing head manufacturing facilities, which annually produce hundreds of millions of thin-film heads. The process includes high-aspect-ratio transformer-coupled plasma (TCP) reactive-ion etching (RIE), which achieves a 20:1 height-to-width aspect ratio on 40-mm-thick polymers. The etched polymers are in turn used as molds to fabricate, through a metal electroplating process, high-aspect-ratio invar (a nickel–iron-based alloy) micro-structures. Area-efficient electrostatic rotational MAs have been successfully designed and fabricated using this process. Fig. 1 shows a photograph of such a device mounted on an integrated lead suspension.

A pico-slider is attached on top of the MA. Electrical contacts between the slider and MA are made using laser reflow. The electrostatic MA is assembled on to the gimbal of an integrated lead suspension and rotates the pico-slider about its center of mass, using an area-efficient layout of electrostatically actuated comb-fingers.

Since the pico-slider flies on top of the disk on an air bearing, the MA must support a gram of out-of-plane loading, with minimum out-of-plane deflection. Thus, the MA's flexures must be very stiff in the out-of-plane direction while compliant in the in-plane radial direction in order to have enough dc gain. A 400:1 out-of-plane/in-plane stiffness ratio was achieved by the 20:1 height–width flexure aspect ratio in the fabrication process described above. Because of out-of-plane deflection constraints,

TABLE I
IBM'S ELECTROSTATIC MA PARAMETERS

Res. Freq. ω_{MO}	Damping Coeff. ζ_{MO}	Stroke limit	Acc. Gain A_M	Max. Voltage
1.5 kHz $\pm 15\%$	0.015	$\pm 1\ \mu m$	2 G/V	± 40 V

the combined MA pico-slider assembly was designed to have a nominal in-plane rotational flexural resonance frequency of 1.5 kHz. Variations in the etching process and lithographic misalignments cause $\pm 15\%$ variations in the MA's resonance frequency from its designed nominal value. Besides this single lightly damped resonance mode, the MA does not have other appreciable structural dynamics up to the 40-kHz frequency range. Thus, its dynamics can be adequately described by a simple mass-spring-damper second-order transfer function [1], [3]

$$G_M(s) = \frac{A_M}{s^2 + 2\zeta_{MO}\omega_{MO}s + \omega_{MO}^2}. \tag{1}$$

Table I provides values for the parameters in (1) as well as other important parameters of the IBM MA model, on which the designs in this paper are based.

A rotational MA design was selected, in order to counteract the hundreds of G in plane acceleration that is exerted to the pico-slider's center of mass by the voice coil motor (VCM) during a seek operation. The pico-slider is mounted on the MA in a way that its center of mass coincides with the actuator's axis of in-plane rotation. Considering VCM as a rigid body,[1] the equations of motion of the dual-stage system are

$$J_V^* \ddot{\theta}_V = \tau_V - J_M \ddot{\theta}_M \tag{2}$$

$$J_M \ddot{\theta}_M + B_M \dot{\theta}_M + K_M \theta_M = \tau_M - J_M \ddot{\theta}_V \tag{3}$$

where

$$J_V^* = J_V + J_M + M_M l^2 \tag{4}$$

and J_V and J_M are, respectively, the moment of inertia of the VCM and the MA, M_M is the mass of the MA, l is the distance between the mass center of the MA and the pivot of the VCM, θ_V is the angular position of the VCM, θ_M is the angular position of the MA relative to the VCM, τ_V is the torque input to the VCM, τ_M is the torque produced by the MA, B_M is the damping coefficient of the MA, and K_M is the stiffness of the MA. Given the fact that the inertia of the MEMS MA is very small compared to that of the VCM, $(J_M/J_V) = 1.1e - 7$ for the model used in this paper, we can neglect the coupling term $J_M \ddot{\theta}_M$ in (2) and assume that motion of the MA has no effect on the motion of the VCM. Equation(3) can be rewritten as

$$J_M^* \ddot{\theta}_M + B_M \dot{\theta}_M + K_M \theta_M = \tau_M^* \tag{5}$$

where

$$J_M^* = J_M \left(1 - \frac{J_M}{J_V^*}\right), \quad \tau_M^* = \tau_M - \frac{J_M}{J_V^*}\tau_V. \tag{6}$$

Equation (6) shows that the motion of the MA can be decoupled from the VCM by feeding τ_V to the MA with a proper

[1]Through this paper, we will refer to the combined VCM, E-block, and suspension assembly as VCM. The assumption that the VCM is a rigid body in this section is to simplify the dynamics analysis. In the subsequent section, it includes the resonance modes of the E-block and suspension.
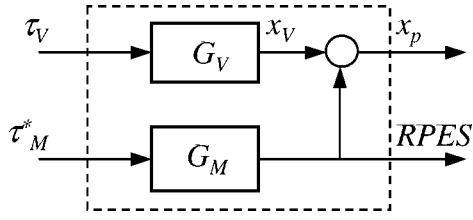
Fig. 2.   Dual-stage block diagram.

Fig. 3.   Dual-stage control design block diagram.

Fig. 4.   The sensitivity block diagram.

gain. As a consequence, for controller design purposes, the dual-stage system can be approximated by the block diagram shown in Fig. 2, where G_V and G_M are, respectively, the VCM and MA transfer functions (TF), x_P is the absolute position of the read/write head, and x_v is the absolute position of the tip of the suspension). Thus, x_P is the summation of x_v and the position of the MA relative to the suspension, which will be referred to in this paper as $RPES$, and is defined as

$$x_p = x_v + RPES. \qquad (7)$$

The controller design in this paper is based on this dual-stage model. For implementation, the actual control torque to the MA is given by

$$\tau_M = \tau_M^* + \frac{J_M}{J_V^*}\tau_V \qquad (8)$$

where τ_M^* and τ_V are generated from the designed controller.

Capacitive sensing can be used in MEMS electrostatic MAs to measure the $RPES$ [2]. However, this requires additional sensing electronics and wires to and from the head gimbal assembly (HGA), which may result in an unacceptable increase in the fabrication and assembly costs. Thus, whether or not the $RPES$ will be used in MEMS dual-stage servo systems is still an open question. In this paper, we will classify dual-stage track-following controllers into two categories, according to the availability of the $RPES$: those utilizing the $RPES$ will be called multi-input–multi-output (MIMO) controllers, while those not utilizing the $RPES$ will be called single-input–multi-output (SIMO) controllers.

III. DECOUPLED TRACK-FOLLOWING CONTROLLER DESIGN

The block diagram for a MIMO decoupling control design proposed in this paper is shown in Fig. 3.

The part enclosed in the dashed box on the upper-right corner of Fig. 3 is the open loop system described in Fig. 2. r represents the track runout, PES is position error signal of the head relative to the data track center (i.e., $PES = r - x_P$), while $RPES$ is the position error signal of the head relative to the tip of the suspension (i.e., $RPES = x_P - x_v$).

The decoupling control approach, originally introduced by [10], utilizes the PES and $RPES$ to generate the position error of the suspension tip relative to the data track center, which will be labeled as $VPES$

$$VPES = PES + RPES = r - x_v \qquad (9)$$

and this signal is fed to the VCM loop compensator.[2]

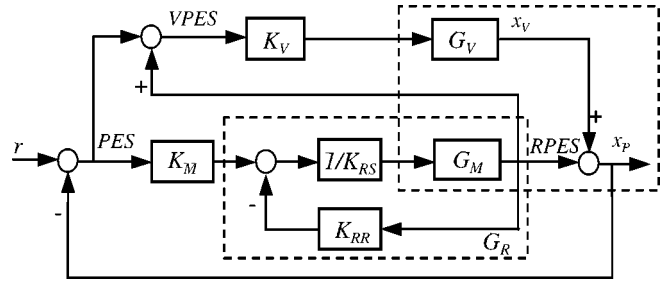[2]In [10], the $RPES$ was not assumed to be available and was estimated with an open loop observer gain.
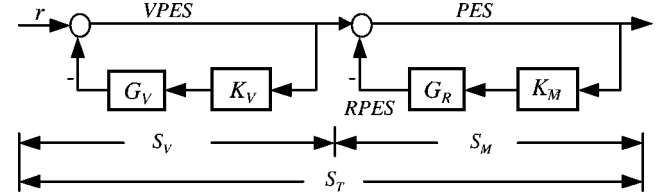
In the block diagram shown in Fig. 3, there are three compensators that need to be designed: the VCM loop compensator K_V, the MA PES loop compensator K_M, and the MA $RPES$ minor loop compensator K_{RR}/K_{RS}. K_{RR}/K_{RS} is used to damp the MA's flexure resonance mode and place the closed-loop poles of the MA $RPES$ loop at an appropriate location. The damped MA closed-loop transfer function G_R, shown in the lower-middle dashed box, is defined as

$$G_R = \frac{G_M}{K_{RS} + G_M K_{RR}} \qquad (10)$$

while the total dual-stage open loop TF from r to x_P, G_T, is given by

$$G_T = K_V G_V + K_M G_R + K_M G_R K_V G_V. \qquad (11)$$

The block diagram in Fig. 3 is equivalent to the sensitivity block diagram shown in Fig. 4, and the total closed-loop sensitivity TF from r to PES is the product of the VCM and MA loop sensitivity TFs, respectively, S_V and S_M:

$$S_T = \frac{1}{1 + G_T} = S_V S_M \qquad (12)$$

where

$$S_V = \frac{1}{1 + K_V G_V}, \quad S_M = \frac{1}{1 + K_M G_R}. \qquad (13)$$

Thus, the dual-tage servo control design can be decoupled into two independent designs: the VCM loop, whose error rejection loop sensitivity TF is given by S_V in (13), and the MA loop, whose error rejection loop sensitivity TF is given by S_M in (13).

A. VCM Closed-Loop Sensitivity S_V

The VCM loop compensator K_V is designed to attain a desired VCM closed loop sensitivity S_V. Its bandwidth is generally limited by the E-block and suspension resonance modes. The design of this compensator can be accomplished using conventional SISO frequency shaping techniques and will not be discussed here in detail. For illustration purposes, a sixth-order model of the VCM, which includes torsional and sway vibration modes of the suspension at 2.4 and 5 kHz, respectively, was utilized in our simulation study and a fourth-order compensator
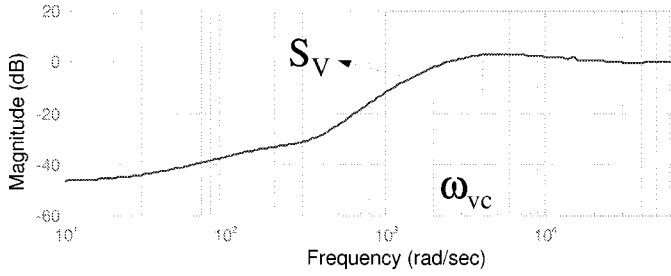
Fig. 5.   VCM loop sensitivity S_V magnitude bode plot.

K_V running at a 20-kHz sampling rate was designed to have an approximated bandwidth of $\omega_{VC} = 500\,\mathrm{Hz}$. The gain Bode plot of the resulting sensitivity TF S_V is shown in Fig. 5.

B. MA Closed-Loop Sensitivity S_M

The MA loop controller is designed to increase the overall closed-loop sensitivity attenuation. This design process is explained in detailed in Section III-C, after we review the pole placement design method applied to the MEMS MA.

1) MA RPES Minor Loop Controller Design by Pole Placement: The zeroth-order-hold discrete time transfer function for the MA model given in (1) is

$$G_M(q^{-1}) = \frac{q^{-1}B_o(q^{-1})}{A_o(q^{-1})} \qquad (14)$$

where q^{-1} is a one-step delay operator and $B_o(q^{-1})$ and $A_o(q^{-1})$ are, respectively, the MA open loop zero and pole polynomials

$$B_o(q^{-1}) = b_o(1 + z_o q^{-1}), \qquad (15)$$

$$A_o(q^{-1}) = 1 + a_1 q^{-1} + a_2 q^{-2}, \qquad (16)$$

$$a_1 = -2p_o \cos(\omega_{do}T), \quad a_2 = p_o^2 \qquad (17)$$

$$z_o = \frac{p_o(p_o + (\sigma_o/\omega_{do})\sin(\omega_{do}T)\cos(\omega_{do}T))}{1 - p_o(\cos(\omega_{do}T) + (\sigma_o/\omega_{do})\sin(\omega_{do}T))} \qquad (18)$$

$$\sigma_o = \zeta_{MO}\omega_{MO}, \quad p_o = e^{-\sigma_o T} \qquad (19)$$

$$\omega_{do} = \omega_{MO}\sqrt{1 - \zeta_{MO}^2} \qquad (20)$$

where T is the controller sampling time and ω_{MO} and ζ_{MO} are, respectively, the MA's natural frequency and damping ratio, given by Table I.

Consider now the $RPES$ minor loop feedback system enclosed by the dashed box in the lower part of Fig. 3 and the resulting MA closed-loop TF $G_R(q^{-1})$ defined by (10). Its poles can be placed by solving the following Diophantine equation [11]:

$$A_R(q^{-1}) = A_o(q^{-1})K_{RS}(q^{-1}) + q^{-1}B_o(q^{-1})K_{RR}(q^{-1}), \qquad (21)$$

The closed-loop polynomial $A_R(q^{-1})$ in (21) is chosen by the designer and its roots are the damped MA poles. It is convenient to define the second-order polynomial $A_R(q^{-1})$ in an analogous manner to the open loop polynomial $A_o(q^{-1})$ in (16), in terms of the equivalent continuous time natural frequency ω_{MR} and damping ratio ζ_{MR}, (i.e., substitute ω_{MO} and ζ_{MO}, respectively, by ω_{MR} and ζ_{MR} in (17)–(20)).

ω_{MR} is a design parameter which will be specified later on and normally $\zeta_{MR} \geq 1$. When $A_R(q^{-1})$ is second order, the
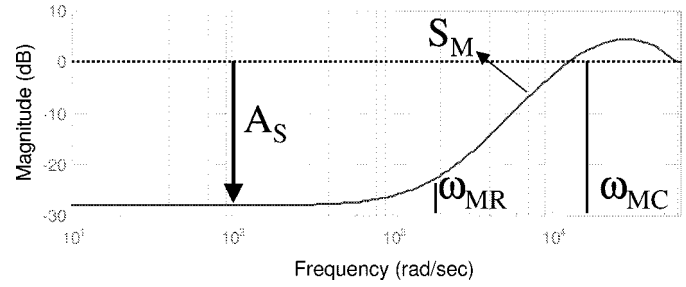
$RPES$ minor loop polynomials $K_{RS}(q^{-1})$ and $K_{RR}(q^{-1})$ are both first-order. The resulting closed-loop transfer function G_R is given by

$$G_R = \frac{q^{-1}B_o(q^{-1})}{A_R(q^{-1})}. \qquad (22)$$

2) MA Outer Loop Controller Design by Pole Placement: Consider now the design of the MA outer loop compensator $K_M(q^{-1}) = K_{MR}(q^{-1})/K_{MS}(q^{-1})$ and assume that the $RPES$ closed-loop transfer function G_R is given by (22). The resulting MA closed-loop sensitivity transfer function S_M, which was defined in (13), is given by

$$S_M(q^{-1}) = \frac{A_R(q^{-1})K_{MS}(q^{-1})}{A_M(q^{-1})} \qquad (23)$$

where the MA outer loop closed-loop polynomial $A_M(q^{-1})$ must be chosen by the designer. The MA outer loop compensator $K_M(q^{-1}) = K_{MR}(q^{-1})/K_{MS}(q^{-1})$ can be designed by solving the following Diophantine equation:

$$A_M(q^{-1}) = A_R(q^{-1})K_{MS}(q^{-1}) + q^{-1}B_o(q^{-1})K_{MR}(q^{-1}). \qquad (24)$$

As in Section III-B1, it is convenient to define the second-order polynomial $A_M(q^{-1})$ in terms of the equivalent continuous time natural frequency ω_{MC} and damping ratio ζ_{MC} · $\omega_{MC} > \omega_{MR}$ and normally $\zeta_{MC} \geq 1$.

For $\zeta_{MR} = \zeta_{MC} = 1$, the low-frequency attenuation of S_M is given by

$$A_S = \left(\frac{1 - p_{MR}}{1 - p_{MC}}\right)^2 \left[1 + z_o - z_o \left(\frac{z_o + p_{MC}}{z_o + p_{MR}}\right)^2\right] \qquad (25)$$

where z_o is the open loop MA zero given by (18), $p_{MR} = e^{-\omega_{MR}T}$, $p_{MC} = e^{-\omega_{MC}T}$, and T is the sampling time. Notice that $\lim_{T \to 0} A_S = (\omega_{MR}/\omega_{MC})^2$. Thus, the ratio $(\omega_{MR}/\omega_{MC})^2$ can be used to roughly determine the increased attenuation provided by the MA.

The gain Bode plot of the sensitivity TF S_M is shown in Fig. 6, for the case when $\omega_{MC} = 2.4\,\mathrm{kHz}$, $\omega_{MR} = 300\,\mathrm{MHz}$, $\zeta_{MR} = \zeta_{MC} = 1$, and a 20-kHz sampling rate.

C. Dual-Stage Closed-Loop Sensitivity S_T

The MIMO dual-stage servo system depicted in Fig. 3 can be designed by a three-step design process, which is based on (12)–(25), and is schematically illustrated by Fig. 7.

First, the VCM compensator K_V is designed to attain a desired VCM closed-loop sensitivity S_V. In a typical design, the VCM bandwidth ω_{VC} in Fig. 7 is limited by the existence of E-block and suspension resonance modes to be between

Fig. 6.   MA loop sensitivity S_M magnitude Bode plot.

Fig. 7. Illustration of dual-stage sensitivity S_T design.

Fig. 8. SIMO control design block diagram.

results in an unnecessary decrease in attenuation A_S. We proposed that ω_{MR} be initially chosen to be the same as ω_{VC}. It can subsequently be adjusted so that the desired attenuation and phase margin requirements of the overall dual-stage system are met. Decreasing ω_{MR} increases the low-frequency attenuation of S_T. However, this generally reduces the phase margin of the overall open loop transfer function G_T in (11).

D. SIMO Track-Following Controller Design

The design procedure describe above can also be applied to SIMO control architectures, where the $RPES$ is not available, by incorporating an open loop observer to estimate the $RPES$, as shown in Fig. 8. In this case, the open loop observer G_R, as defined in (22), generates the $RPES$ estimate signal $\hat{RPES}$.

By (21), the combined action of the open loop observer G_R and the $RPES$ minor loop compensator K_{RS}/K_{RR} is equivalent to the notch filter, K_{MN}, which is defined by

$$K_{MN}(q^{-1}) = \frac{1}{K_{RS}}(1 - G_R K_{RR}) = \frac{\hat{A}_o(q^{-1})}{A_R(q^{-1})} \qquad (26)$$

where $\hat{A}_o(q^{-1})$ is the nominal MA open loop pole polynomial, and $A_R(q^{-1})$ is the desired pole polynomial of G_R.

Ideally, if $\hat{A}_o(q^{-1}) = A_o(q^{-1})$, the notch filter cancels the MA open loop poles and assigns the poles defined by $A_R(q^{-1})$. However, the stability of the system is very sensitive to the uncertainty in the lightly damped MA resonance frequency, ω_{MO}. In order to make the notch filter K_{MN} more robust to the variations in ω_{MO}, a "wider" notch filter can be used by setting a larger damping ratio for $\hat{A}_o(q^{-1})$. However, this will degrade the performance of system, as shown in the step response in the next section. A better method for compensating the variations in the MA resonance frequency is to identify the MA poles online and then generate the controller using the identified model. In Section V-B, we introduce an online identification method that does not require the $RPES$ sensing.

E. Design and Simulation Results

In this section, we show simulation results of the proposed MIMO and SIMO designs, when the PES sampling frequency is 20 kHz. Fig. 9 shows the gain Bode plot of the closed-loop sensitivity TF from track runout r to PES, for both the MIMO and SIMO designs. The design parameters used in the simulations were $\omega_{VC} = 500$ Hz, $\omega_{MR} = 300$ Hz, $\zeta_{MR} = 1$, $\omega_{MC} = 3000$ Hz, and $\zeta_{MC} = 1$. In the case of the MIMO design, K_V

400–700 Hz. Subsequently, the MA compensators are designed to attain the additional attenuation, A_s, provided by the MA closed-loop sensitivity S_M. As discussed in Section III-B, this is accomplished by a two-step process. First, the minor $RPES$ loop compensators, K_{RR}/K_{RS}, are designed in order to damp the MA resonance mode and place the poles of G_R, at a desired location. This involves the solution of the Diophantine (24). Since the poles of G_R become zeros of S_M, this is equivalent to placing the first corner frequency ω_{MR} of S_M in Fig. 7. Finally, the PES loop compensator K_M is designed to determine the overall bandwidth ω_{MC} of the MA loop closed-loop sensitivity S_M. This can also be achieved by pole placement or other loop-shaping techniques.

ω_{MC} is limited by the PES sampling frequency, which is assumed to be 20 kHz in this paper, and the controller computational time delay, which was estimated to be 1/3 the controller sampling time. In [13], guidelines were developed for determining the allowable servo bandwidth based on the available sampling time and the computational delay time and suggest a bandwidth ω_{MC} of approximately 2.5 kHz for the above mentioned sample rate and time delay.

The total dual-stage sensitivity S_T is schematically shown in the bottom part of Fig. 7. For a given PES sampling rate and time delay, and thus the bandwidth ω_{MC}, the additional attenuation A_S provided by the MA loop will be determined by the selection of the $RPES$ lower corner frequency ω_{MR}. Since selecting ω_{MR} to be larger than the VCM loop bandwidth, ω_{VC}
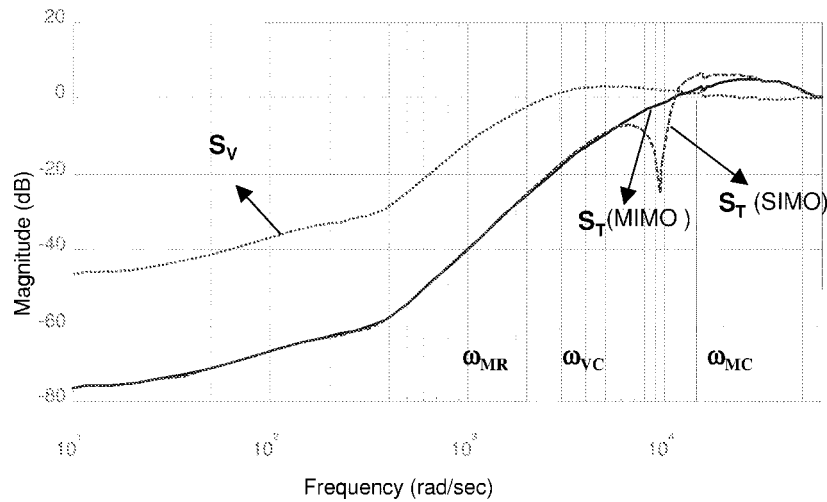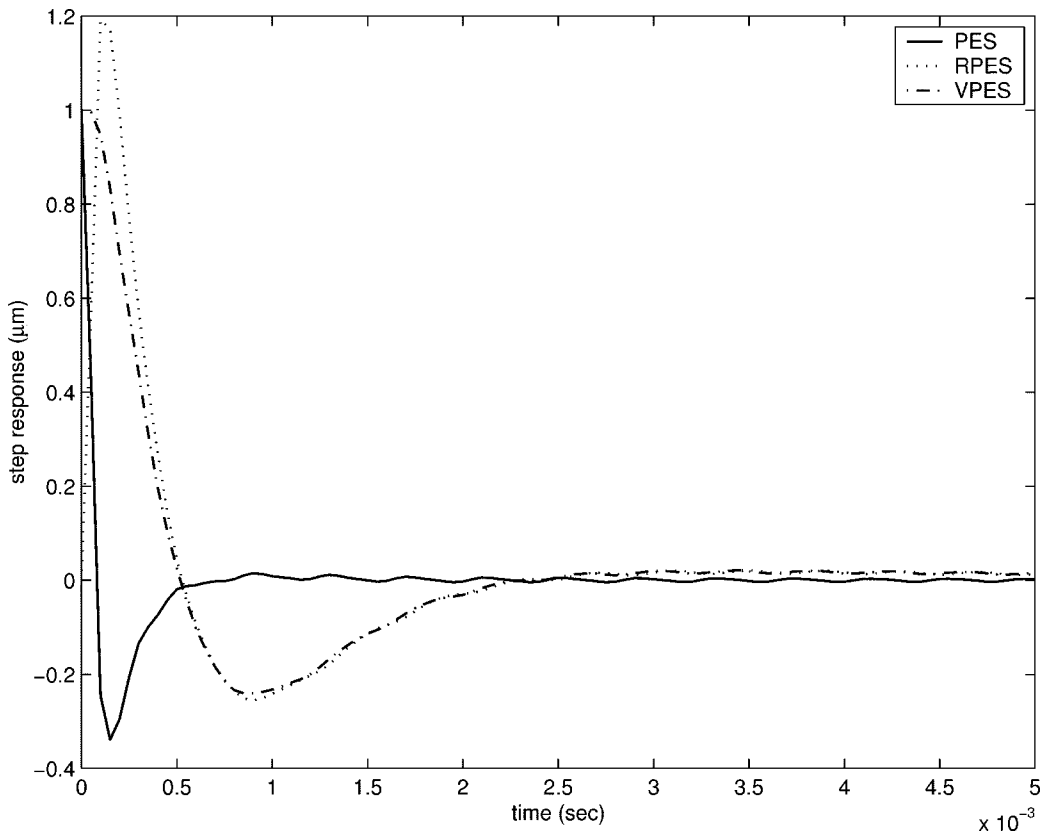
Fig. 9. S_V and S_T magnitude Bode plot.

Fig. 10.   Step response of MIMO design.

is fourth order, both K_M and K_{RS}/K_{RR} are first order. The gain crossover frequency (GCF), gain margin (GM), and phase margin (PM) of open loop TF from r to x_p are, respectively, 2337 Hz, 9.1 dB, and $42.3°$. In the case of the SIMO design, the combined VCM loop compensator is fifth order, and the combined MA loop compensator is fourth order. When the damping ratio of $\hat{A}_o(q^{-1})$ was set to be 10 times larger than the MA TF, the GCF, GM, and PM of open loop TF from r to x_p are, respectively, 2432 Hz, 8.7 dB, and $24.7°$. Figs. 10 and 11 respectively show the 1-μm time-domain step responses of the MIMO

and SIMO designs. The SIMO controller response has a larger overshoot and exhibits more residual vibrations than the MIMO controller response. This is due to the fact that the MA's resonance poles are not being exactly canceled by the notch filter K_{MN} in (26), in order to guarantee the stability robustness of the designed controller to MA resonance frequency variations.

Notice that the settling time of the step response is relatively long. A decoupled dual-stage feedforward control can be used to reduce the overshoot and settling time for track seeking [12].
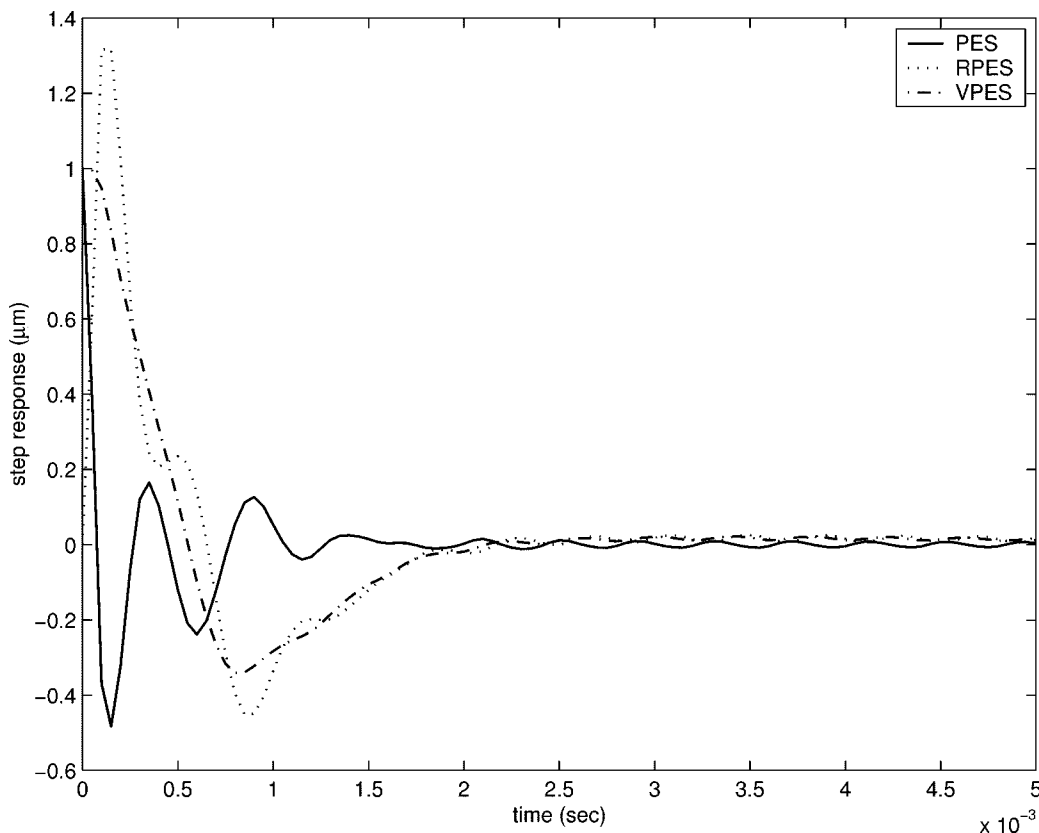
Fig. 11. Step response of SIMO design.

IV. ROBUST STABILITY ANALYSIS USING μ

The robustness of the decoupled MIMO and SIMO designs presented in Section III can be analyzed using the μ-analysis [14]. μ, the structured singular value, is a measure of how big a perturbation to a system must be in order to make the closed-loop system unstable. For the case of MEMS-based dual-stage servo systems, we are particularly concerned with the robustness of the closed-loop system to variations in the resonance frequency (or equivalently the stiffness) of the MA, unmodeled high-frequency structural resonance modes of the VCM actuator, and variations in the dc gain of the VCM. In the μ robust stability analysis framework, model uncertainties are represented using linear fractional transformations (LTF). Fig. 12 shows the block diagram that was used to describe structured uncertainties in our system. Three model uncertainties δ_1, δ_2, and δ_3 are considered in Fig. 12: δ_1 represents the additive uncertainty used to describe the VCM unmodeled resonance dynamics and W_{UV} is the frequency-shaped weight for δ_1. An uncertainty with the size of the amplitude of the biggest resonance peak of the VCM model was used for δ_1. δ_2 is the parameter uncertainty that represents VCM loop gain variations. δ_3 is the parameter uncertainty that represents MA stiffness variations. We assume that both the VCM dc gain and the MA resonance frequency can change by $\pm10\%$ from their respective nominal values.

Fig. 13 shows the resulting robust stability μ plots. It shows a peak μ value of $\beta_{\text{MIMO}} = 0.18$ for the MIMO design and
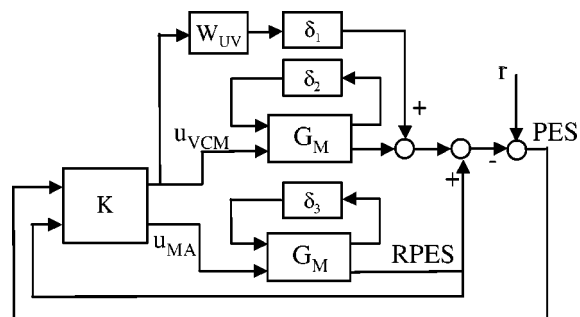
Fig. 12. μ-synthesis design block diagram.

a peak μ value of $\beta_{\text{SIMO}} = 0.49$ for the SIMO design. Thus, both designs can maintain stability for the structured uncertainties described above and the MIMO design has better stability robustness than the SIMO design, as expected.

Of these three structured uncertainties, it is the variations in the MA's stiffness which appear to have the most significant detrimental effect on the performance of both the MIMO and SIMO designs, even when the closed-loop system remains stable. For the MIMO design, variations in the stiffness of the MA's flexures produce variations in its dc gain. These dc gain variations have a large effect on the gain of the open loop transfer function G_T, which is dominated at low frequencies by the last term of (11). For the SIMO design, the lightly damped MA resonance mode can be excited if there is a significant mismatch between the actual MA resonance frequency and its nominal value.
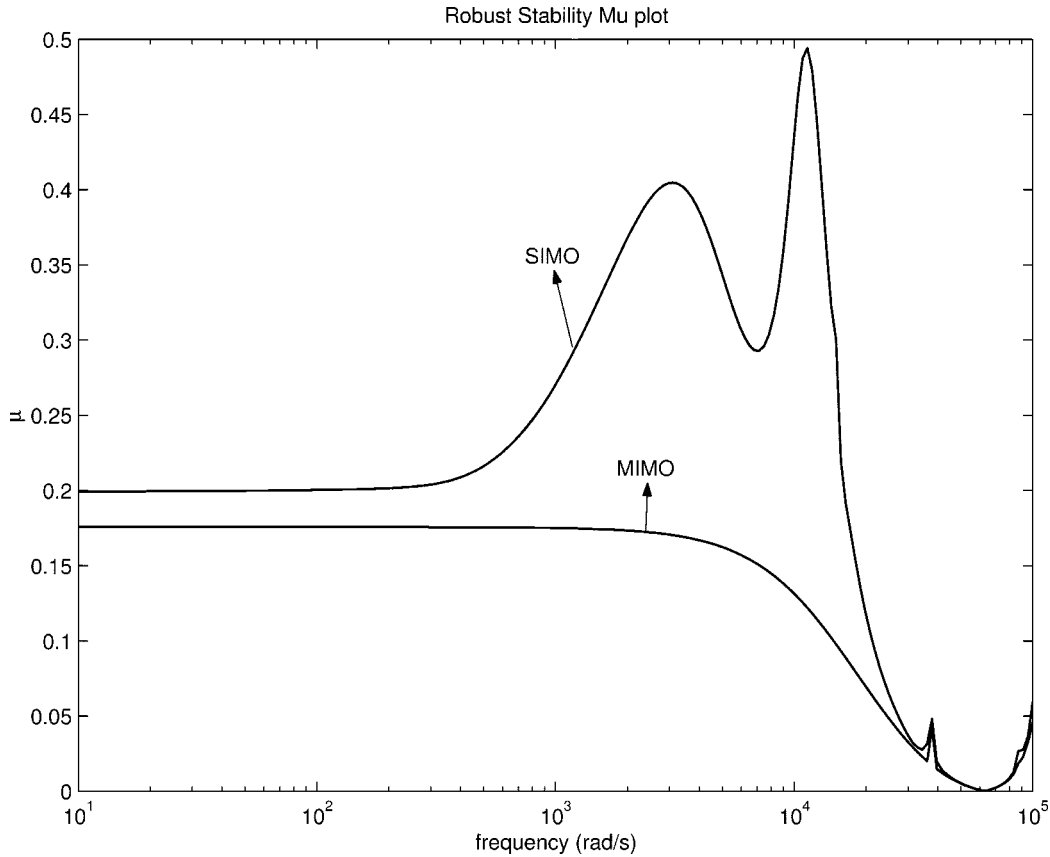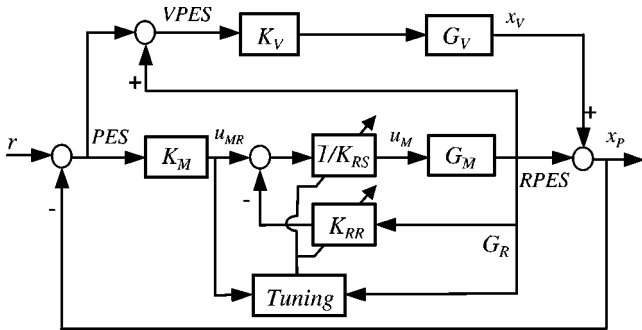
Fig. 13. Stability μ plot.

Fig. 14. Self-tuning control of the MA.

V. COMPENSATION OF THE VARIATIONS IN THE MA'S RESONANCE MODE

Two adaptive schemes are developed for compensating the variations in the MA's resonance mode. The first one utilizes a direct self-tuning algorithm to tune the MA $RPES$ inner loop controller, which can be applied to the MIMO design. For the second method, the open loop MA model parameters are first identified, and the control parameters are subsequently computed with pole placement based on the identified MA parameters. This scheme is applicable to both the MIMO and SIMO designs.

A. RPES Inner Loop Self-Tuning Control

The block diagram for the MA inner loop self-tuning control is shown in Fig. 14. The parameter adaptation algorithm (PAA)

that will be presented is based on the pole placement design and requires measurement of the MA's relative position error signal $RPES$.

Consider the MA open loop transfer function in (14). Since the MA's resonance mode is lightly damped, the zero z_o in (15) and (18) remains fairly invariant with $\pm15\%$ variations in the resonance frequency ω_{MO} and, moreover, $z_o \approx 1$. Thus, it is possible to factor out the "known" term $(1 + z_o q^{-1})$ from the Diophantine equation (21).

The resulting minor-loop $RPES$ closed-loop dynamics is given by

$$
\begin{aligned}
A_c(q^{-1})y(k) =& q^{-1}b_0(1 + z_o q^{-1}) \\
& \times \left[K_{RS}(q^{-1})u_{MR}(k) + K_{RR}(q^{-1})y(k) \right]
\end{aligned}
$$
(27)

where u_{MR} is the control input to the MA and y denotes the position of the MA relative to the VCM, i.e., $y = RPES$. Defining

$$ S(q^{-1}) = b_0 K_{RS}(q^{-1}) = s_0 + s_1 q^{-1}, \qquad (28) $$

$$ R(q^{-1}) = b_0 K_{RR}(q^{-1}) = r_0 + r_1 q^{-1}, \qquad (29) $$

the regressor vector $\phi(k)$ and filtered regressor vector $\phi_f(k)$ as

$$ \phi(k) = [u_{MR}(k)\ u_{MR}(k-1)\ y(k)\ y(k-1)] $$
(30)

$$ A_c(q^{-1})\phi_f(k) = (1 + z_o q^{-1})\phi(k) \qquad (31) $$

and the controller parameter vector $\theta = [s_0\ s_1\ r_0\ r_1]^{\mathrm{T}}$, the closed-loop $RPES$ dynamics (27) can be rewritten as

$$ y(k) = \theta^{\mathrm{T}} \phi_f(k-1). \qquad (32) $$
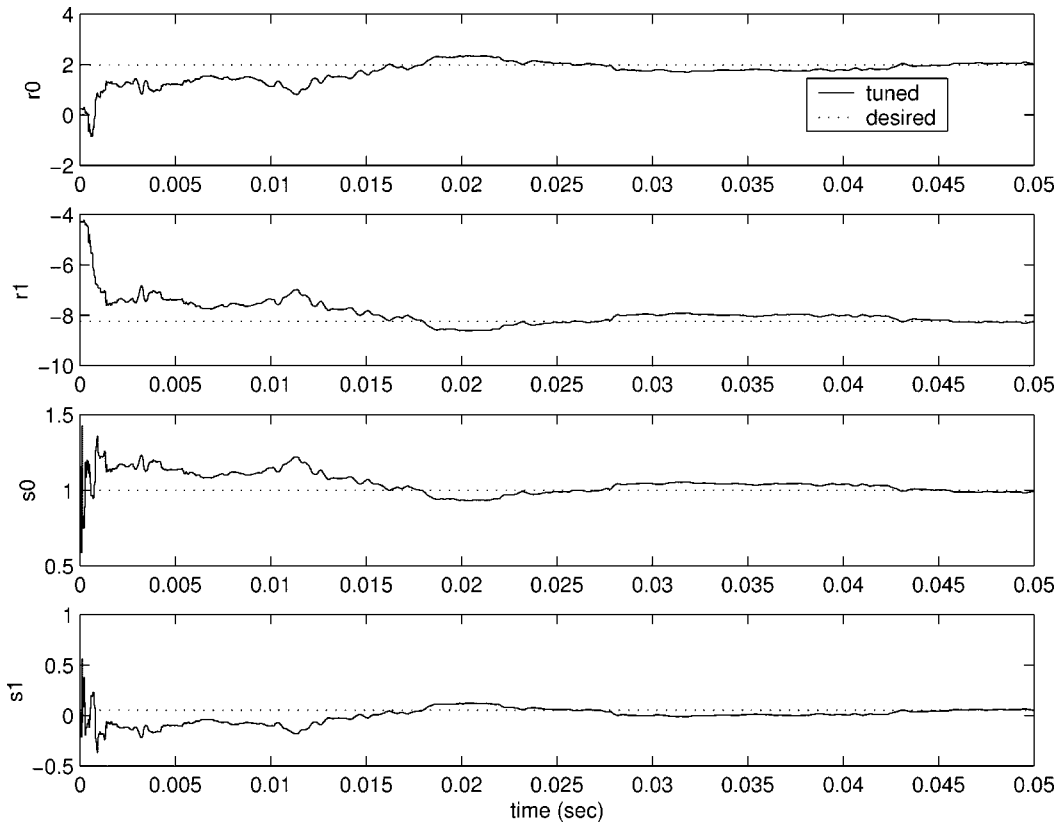
Fig. 15.   Control parameters adaptation response.

From (32), the controller parameter vector estimate $\hat{\theta}(k) = [\hat{s}_0(k)\ \hat{s}_1(k)\ \hat{r}_0(k)\ \hat{r}_1(k)]^{\mathrm{T}}$ can be updated using a standard recursive least square algorithm (RLS) [11]

$$\hat{\theta}(k) = \hat{\theta}(k-1) + P(k)\phi_f(k)e^o(k) \qquad (33)$$

$$e^o(k) = y(k) - \hat{\theta}^{\mathrm{T}}(k-1)\phi_f(k-1) \qquad (34)$$

$$P(k) = \left[P(k-1) \right.$$
$$\left. - \frac{P(k-1)\phi_f(k-1)\phi_f^{\mathrm{T}}(k-1)P(k-1)}{1+\phi_f^{\mathrm{T}}(k-1)P(k-1)\phi_f(k-1)} \right]. \qquad (35)$$

The control law is

$$\hat{S}(k,q^{-1})u_{MR}(k) = \hat{s}_o(k)u_M(k) - \hat{R}(k,q^{-1})y(k) \qquad (36)$$

with

$$\hat{S}(k,q^{-1}) = \hat{s}_o(k) + \hat{s}_1(k)q^{-1} \qquad (37)$$

$$\hat{R}(k,q^{-1}) = \hat{r}_o(k) + \hat{r}_1(k)q^{-1} \qquad (38)$$

and $u_{MR}(k)$ the output of the MA fixed outer loop compensator K_M and $u_M(k)$ the control input to the MA.

Fig. 15 shows the simulation of the control parameters estimates using the RLS algorithm. In the simulation, realistic estimates of the runout, VCM and MA torque disturbances, and PES and $RPES$ measurement noises were injected into the dual-stage system at corresponding locations. A white noise with an rms value of 10 nm was injected to the $RPES$ sensing signal. This noise is mainly due to thermal noise and feed-through in the capacitive sensing electronics [2], [15].
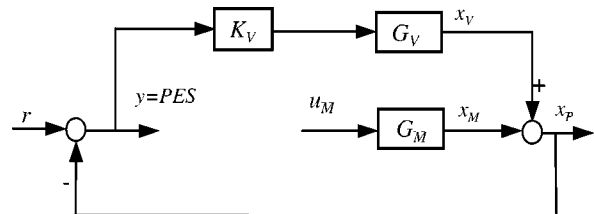

Fig. 16.   MA model identification with no $RPES$ sensing.

Fig. 15 shows the simulation of the controller parameter estimates $\hat{s}_o(k)$, $\hat{s}_1(k)$, $\hat{r}_o(k)$, and $\hat{r}_1(k)$, for the case when the real MA resonance frequency is 1.2 times its nominal value, and the system was subjected to stochastic disturbances, as discussed above. The controller parameters converged to a value, which is very close to their desired value. Similar responses were obtained when the real resonance frequency is 0.8 times the nominal value. If the $RPES$ noise level is too large, the control parameter estimates may not converge to their desired values and other PAA's, such as normalized or extended RLS, can be used for better convergence [11].

B. Online MA Model Identification

Since the variations in the MA's resonance frequency ω_{MO} are due to its fabrication process, and ω_{MO} does not change after the MA has been fabricated, it is feasible to identify the MA open loop dynamics online during the drive's manufacturing and testing stage. The controller parameters can then be subsequently determined, based on the identified MA plant parameters, by solving (21) and (24).
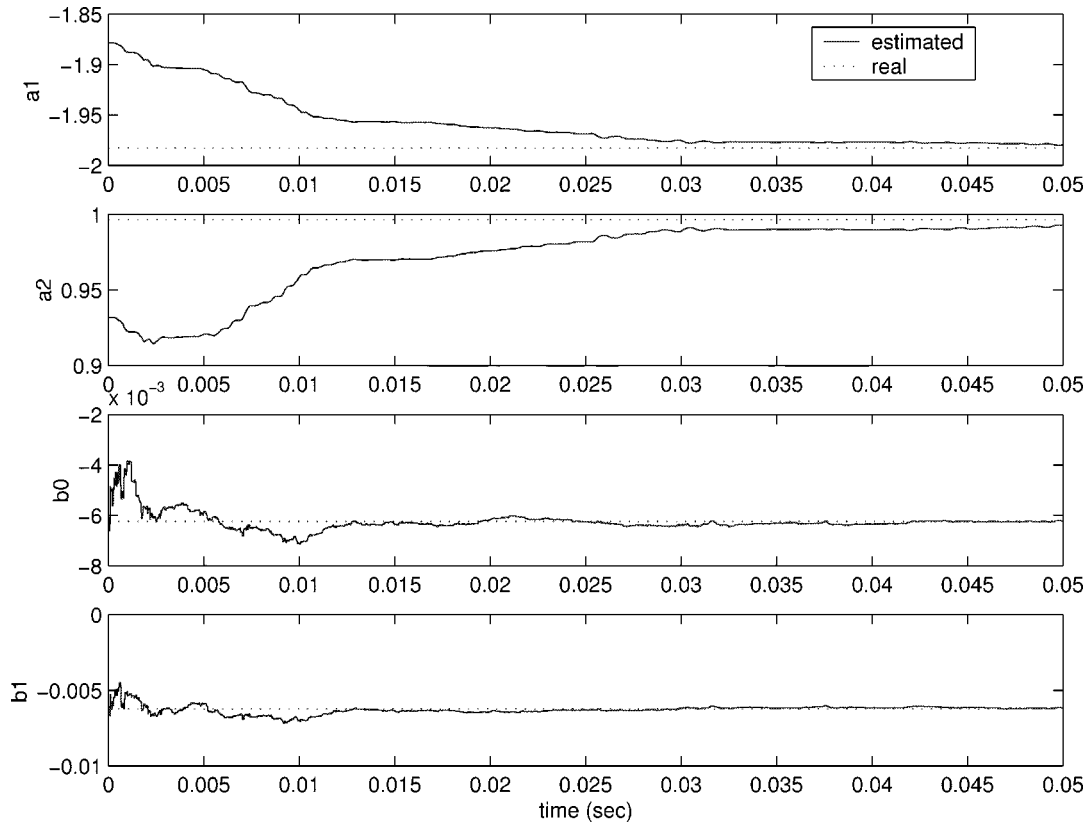
Fig. 17.   Control parameters adaptation responses.

When the $RPES$ is available, the VCM feedback loop can be closed using the $VPES$ as defined in (9). The open loop MA dynamics can be identified by feeding an excitation input signal of a sufficiently large magnitude to the MA. Since the decoupling control structure of the dual-stage servo system prevents the VCM motion from exciting the MA dynamics, the identification of the MA open loop model parameters can be carried out using standard identification techniques, based on the model

$$A_o(q^{-1})y(k) = q^{-1}B_o(q^{-1})u_M(k) + w(k) \qquad (39)$$

where $u_M(k)$ is the input excitation signal to the MA, A_o, B_o are its open loop pole and zero polynomials, as defined in (14), $y(k)$ is $RPES$ and $w(k)$ is $RPES$ measurement noise.

When $RPES$ sensor is not available and the only available feedback signal is the PES, it is still possible to identify the MA open loop dynamics by closing the VCM loop with PES, and feeding an excitation input signal of a sufficiently large magnitude to the MA, as shown in Fig. 16.

Defining this time $y(k)$ to be the PES, we obtain

$$y(k) = G_M u_M^f(k) + S_V r(k) \qquad (40)$$
$$u_M^f(k) = -S_V u_M(k) \qquad (41)$$

where $u_M(k)$ is the input excitation signal to the MA, S_V is the VCM loop sensitivity TF defined in (13), $r(k)$ is the runout and G_M is MA TF. By the spectral factorization theorem, the dynamics in (40) can modeled by

$$A_o(q^{-1})y(k) = q^{-1}B_o(q^{-1})u_M^f(k) + C(q^{-1})w(k) \qquad (42)$$

where A_o, B_o are the MA open loop pole and zero polynomials, which need to be identified, $w(k)$ is a fictitious white noise, and the Hurwitz polynomial $C(q^{-1})$ represents the combined effect of runout, VCM and MA torque disturbances, and PES measurement noise.

Fig. 17 shows the simulation of the MA parameters estimates $\hat{a}_1$, $\hat{a}_2$, $\hat{b}_o$, and $\hat{b}_1$ using the extended recursive least square (ERLS) algorithm [11]. In the simulation, realistic estimates of the runout, VCM and MA torque disturbances, and PES measurement noise were injected into the dual-stage system at corresponding locations. u_M was a white excitation with a sufficiently large amplitude to generate about ± 1–μm of MA motion and $\hat{C}(q^{-1})$ was chosen to be fourth order. As shown in Fig. 17, the parameters estimates converged to their true values.

VI. Conclusion

MIMO and SIMO track-following controllers for MEMS-based dual-stage servo systems were designed using a decoupled discrete time pole placement design methodology. Both designs are robust to variations in the MA's resonance frequency. The MIMO design can achieve a superior robustness and performance, partly due to the additional $RPES$ sensor. The decoupled MIMO design presented in this paper requires considerable fewer computations than the μ synthesis design in [9]. Self-tuning control, or online estimation of the MA model parameters combined with the pole placement design, can be used to compensate for the variations in the microactuator's resonance frequency, and restore nominal controller performance.

REFERENCES

[1] L. -S. Fan, T. Hirano, J. Hong, P. R. Webb, W. H. Juan, W. Y. Lee, S. Chan, T. Semba, W. Imaino, T. S. Pan, S. Pattanaik, F. C. Lee, I. McFadyen, S. Arya, and R. Wood, "Electrostatic microactuator and design considerations for hdd application," *IEEE Trans. Magnetics*, vol. 35, pp. 1000–1005, Mar. 1999.

[2] D. Horsley, N. Wongkomet, R. Horowitz, and A. Pisano, "Precision positioning using a microfabricated electrostatic actuator," *IEEE Trans. Magnetics*, vol. 35, pp. 993–999, Mar 1999.

[3] T. Hirano, L. -S. Fan, W. Y. Lee, J. Hong, W. Imaino, S. Pattanaik, S. Chan, R. Horowitz, S. Aggarwal, and D. A. Horsley, "High-Bandwidth High-Accuracy Rotary Microactuators for Magnetic Disk Drive Tracking Servos," *IEEE/ASME Trans. Mechatron.*, vol. 3, pp. 156–165, Sept. 1998.

[4] W. Guo, S. Weerasooriya, T. B. Goh, Q. H. Li, C. Bi, K. T. Chang, and T. S. Low, "Dual stage actuators for high density rotating memory devices," *IEEE Trans. Magnetics*, vol. 34, pp. 450–455, Nov. 1998.

[5] S. Koganezawa, Y. Uematsu, and T. Yamada, "Dual-Stage Actuator System for Magnetic Disk Drives Using a Shear Mode Piezoelectric Microactuator," *IEEE Trans. Magnetics*, vol. 35, pp. 988–992, Mar. 1999.

[6] S. J. Schroeck and W. C. Messner, "Dual-stage track-following servo design for hard disk drive," in *Proc. Amer. Control Conf.e*, June 1999, pp. 4122–4126.

[7] X. Hu, W. Guo, T. Huang, and B. M. Chen, "Discrete time LQG/LTR dual-stage controller design and implementation for high track density HDD's," in *Proc. Amer. Control Conf.*, June 1999, pp. 4111–4115.

[8] T. Semba, T. Hirano, and L. -S. Fan, "Dual-Stage Servo Controller for HDD Using MEMS Actuator," *IEEE Trans. Magnetics*, vol. 35, pp. 2271–2273, Sept. 1999.

[9] D. Hernandez, S. -S. Park, R. Horowitz, and A. K. Packard, "Dual-stage track-following servo design for hard disk drive," in *Proc. Amer. Control Conf.*, June 1999, pp. 4188–4121.

[10] K. Mori, T. Munemoto, H. Otsuki, Y. Yamaguchi, and K. Akagi, "A dual-stage magnetic disk drive actuator using a piezoelectric device for a high track density," *IEEE Trans. Magnetics*, vol. 27, pp. 5298–5300, Nov. 1991.

[11] K. J. Åström and B. Wittenmark, *Computer Controlled Systems: Theory and Design*. Englewood Cliffs, NJ: Prentice-Hall, 1984.

[12] M. Kobayashi, T. Yamaguchi, and R. Horowitz, "Track-seeking controller design for dual-stage actuator in megnatic disk drives," in *Proc. Amer. Automatic Control Conf.*, June 2000, pp. 2610–2614.

[13] M. T. Whilte and W. -M Lu, "Hard disk drive bandwidth limitations due to sampling frequency and computational delay," in *Proc. 1999 IEEE/ASME Int. Conf. Intelligent Mechatronics*, Sep. 1999, pp. 120–125.

[14] G. J. Balas, J. C. Doyle, K. Glover, A. Packard, and R. Smith, *m-Analysis and Synthesis ToolBox*: MUSYN Inc. and The MathWorks, Inc., 1995.

[15] N. Wongkomet, "Position Sensing for Electrostatic Micropositioners," Ph.D. dissertation, Univ. of California, Berkeley, 1998.

Yunfeng Li (S'01) received the B.S. and M.S. degrees from Beijing University of Aeronautics and Astronautics, Beijing, China, in 1992 and 1995, respectively. He is currently working toward the Ph.D. degree in the Department of Mechanical Engineering, University of California, Berkeley, CA.

His current research interests include adaptive control, vibration control and mechatronics with applications to disk drive servo.

Roberto Horowitz (M'89) was born in Caracas, Venezuela, in 1955. He received the B.S. degree with highest honors in 1978 and the Ph.D. degree in 1983 in mechanical engineering from the University of California at Berkeley.

In 1982, he joined the Department of Mechanical Engineering at the University of California at Berkeley, where he is currently a Professor. He teaches and conducts research in the areas of adaptive, learning, nonlinear and optimal control, with applications to micro-electromechanical systems (MEMS), computer disk file systems, robotics, mechatronics and intelligent vehicle and highway systems (IVHS).

Dr. Horowitz was a recipient of a 1984 IBM Young Faculty Development Award and a 1987 National Science Foundation Presidential Young Investigator Award. He is a member of ASME.